Structure directing forces in hybrid layered double perovskites containing aromatic organic cations

Joseph T. Race[ε], Tianyu Liu[ε], and Patrick M. Woodward*

Department of Chemistry and Biochemistry, The Ohio State University, 100 W. 18th Avenue, Columbus, Ohio, 43210, United States

ABSTRACT: Hybrid n = 1 Ruddlesden-Popper perovskites with aromatic ammonium cations like benzylammonium (BzA) and phenethylammonium (PEA) have been shown to adopt polar structures and exhibit ferroelectricity, but many of the examples discovered thus far contain either Pb or Cd. Here, we describe the synthesis and structural characterization of four layered halide double perovskites: $(BzA)_4AgBiBr_8$, $(PEA)_4AgBiBr_8$, $(BzA)_4AgInCl_8$, and $(PEA)_4AgInCl_8$. In all four compounds the inorganic layers exhibit a chessboard ordering of Ag^+ and Bi^{3+}/In^{3+} and the layers stack in a coherent pattern that maintains the ordering over three-dimensional space. The octahedra surrounding Ag^+ show a large axial compression, which results in much shorter bonds to the terminal halide ions than to the bridging halide ions, whereas the bismuth- and indium-centered octahedra show only small distortions. There appears to be a competition between polar distortions of the octahedra and octahedral tilting, both of which can optimize hydrogen bonding interactions between the ammonium cations and the inorganic layers. Unlike the Pb- or Cd-containing analogs, the double perovskites seem to favor patterns of octahedral tilting that suppress polar ordering of the organic cations. The packing of the organic cations depends on both their conformational flexibility and the lateral dimensions of the inorganic layer. These forces favor intra-layer edge-to-face interaction between aromatic rings in the three of the four compounds. The lone exception is $(PEA)_4AgBiBr_8$, which forms weak interlayer edge-to-face interactions between aromatic rings and slip-stacked packing within each organic layer.

Introduction

Hybrid (organic-inorganic) layered perovskites span a wide range of compositional space, due in large part to the flexibility of the structure. These structures contain inorganic layers of corner connected metal-halide octahedra, separated by layers of organic cations, typically protonated amines. The inorganic layers undergo distortions to maintain effective hydrogen bonding interactions with organic cations of various sizes, shapes, and degrees of conformational flexibility.[1,2] These distortions provide a knob to tune the electronic structure and thereby impact the optical, electrical, and magnetic properties, but to do so requires an intimate understanding of the various structure directing forces at work in these materials.

The properties and potential applications of hybrid layered perovskites have attracted considerable interest. Within this family one can find materials that exhibit electroluminescence,[3,4] low dimensional magnetism,[5–7] barocaloric effects,[8,9] and ferroelectricity,[10,11] among other properties. Although nearly every physical property of a material is dependent on crystallographic distortions, the conditions needed to realize ferroelectricity may present the biggest challenge for those interested in the rational design of new materials. In hybrid layered perovskites orientational ordering of polar organic cations, octahedral distortions, and octahedral tilting all play an important

role in stabilizing the structure. Controlling the interplay between these forces is crucial to stabilize a polar structure, a necessary criterion for the realization of ferroelectricity.

Perovskite and perovskite-related oxide ferroelectrics like $BaTiO_3$, $PbZr_{1-x}Ti_xO_3$, $Bi_4Ti_3O_{12}$ and $Bi_2SrNb_2O_9$ find widespread use for their dielectric properties.[12–15] However, the brittle nature of these ceramic materials limits their use in flexible devices. Enter hybrid layered perovskite ferroelectrics, where the presence of organic layers makes them less brittle, and therefore, potential replacements for oxide ferroelectrics in applications where flexibility is required. The presence of a spontaneous electric field gradient can also enhance the already favorable optoelectronic properties of halide perovskites, leading to applications that include ferroelectric photovoltaics,[16] self-powered photodetectors,[17] and ultrasensitive X-ray detectors.[18]

Ferroelectricity was first reported in a hybrid layered perovskite in 2015, when Liao, et al. demonstrated that benzylammonium lead chloride $(C_6H_5CH_2NH_3)_2PbCl_4$ was ferroelectric below its Curie temperature of 438 K.[10] Subsequently, ferroelectricity has been reported in nearly 40 different hybrid layered perovskites[19], but the spontaneous polarization of $(BzA)_2PbCl_4$ (P_s = 13 μC·cm^{-2}) has not been topped. It should also be noted that while switching the polarization direction has proven difficult in all-inorganic layered perovskites like $Ca_3Mn_2O_7$,[20–22] this appears to be less problematic in hybrid layered perovskites.[19] However, the enthusiasm for hybrid layered perovskites is somewhat dampened by the fact that over three quarters of the hybrid layered perovskite ferroelectrics reported to date contain lead.[19] The toxicity and environmental regulations associated with the presence of lead add unwanted hurdles to the commercialization of new materials, thereby providing a strong incentive to find lead-free alternatives.

One approach to discovering stable, lead-free halide perovskites is to replace the Pb^{2+} cations with a 50:50 mixture of M^+ and M^{3+} cations. In the 3D perovskite structure this leads to the double perovskite family with composition, $A_2M^+M^{3+}X_6$.[23–25] In hybrid layered perovskites with inorganic layers one octahedron thick, the composition becomes $A'_2M^+_{0.5}M^{3+}_{0.5}X_4$, which for an ordered arrangement of cations is more appropriately written as $A'_4M^+M^{3+}X_8$. Although less common than A'_2BX_4 hybrid layered perovskites, several $A'_4M^+M^{3+}X_8$ hybrid layered double perovskites have been reported.[6,26–29] In this paper, we report the synthesis and characterization of four hybrid layered double perovskites containing either benzylammonium (BzA = $C_6H_5CH_2NH_3^+$) or phenethylammonium (PEA = $C_6H_5CH_2CH_2NH_3^+$) cations. $(BzA)_4AgInCl_8$ and $(PEA)_4AgInCl_8$ are synthesized and studied for the first time, while the crystal structures of $(BzA)_4AgBiBr_8$ and $(PEA)_4AgBiBr_8$ are revisited. By incorporating relatively rigid organic cations with aromatic rings it was hoped that the structure and properties might emulate the ferroelectric $(BzA)_2PbCl_4$. While that expectation was not realized, the crystal chemistry of these phases provide important insight regarding the structure directing forces at work in hybrid layered perovskites.

Symmetry Analysis

To understand the details of the crystal structures studied here, it is useful to review the symmetry consequences of cation ordering and octahedral tilting in layered perovskites. Layered perovskites can be divided into Ruddlesden-Popper (RP), Dion-Jacobson (DJ), and Aurivillius families. The compositions studied here belong to the RP family, a homologous series with the general formula $A'_2A_{n-1}M_nX_{3n+1}$, where n is the number of corner-connected

octahedral layers. The RP structure type is characterized by an offset of ½ *a* + ½ *b* between adjacent layers of corner-connected octahedra in the unit cell, leading to a body centered tetragonal structure with *I*4/*mmm* space group symmetry.[30]

The octahedra that make up the inorganic layers can undergo cooperative distortions by rotating about one or more of the local 4-fold axes of the octahedra, lowering the symmetry of the structure in the process. The symmetry consequences of octahedral tilting were originally studied by Hatch et al.[30] Recently the analysis was revisited and expanded upon by Liu et al.[1] Aleksandrov categorized the tilts/rotations of the octahedra into three different categories: θ-, ϕ-, and ψ-tilts, as shown in Figure 1.[31] The θ-tilts correspond to a rotation of each octahedron about the 4-fold axes that run parallel to the *c*-axis of the parent unit cell (i.e. normal to the layers). The ϕ-tilts correspond to tilts around the *a*- and/or *b*-axes of the parent unit cell. They are characterized as out-of-phase tilts because the sense of the octahedral rotation alternates between clockwise and counterclockwise along the axis of the rotation. The ψ-tilts are also about the *a*- and/or *b*-axes but maintain the same sense along the rotation axis. Consequently, they are referred to as in-phase tilts. They are rarely observed in $n = 1$ RP phases and will not be discussed further in this article. The ϕ-tilts typically occur about both *a*- and *b*-axes and are denoted (ϕϕ0) if θ-tilts are absent or (ϕϕθ) when they are seen in combination with θ-tilts. If the tilts have different magnitudes around the *a* and *b* axes, a subscript is used to denote the inequivalence, for example ($\phi_1\phi_2$0). A bar over the tilt, $\bar{\theta}$ or $\bar{\phi}$, signifies that the direction of the tilt is opposite from one layer to the next. A more thorough description of octahedral tilting in layered perovskites can be found in reference 1.

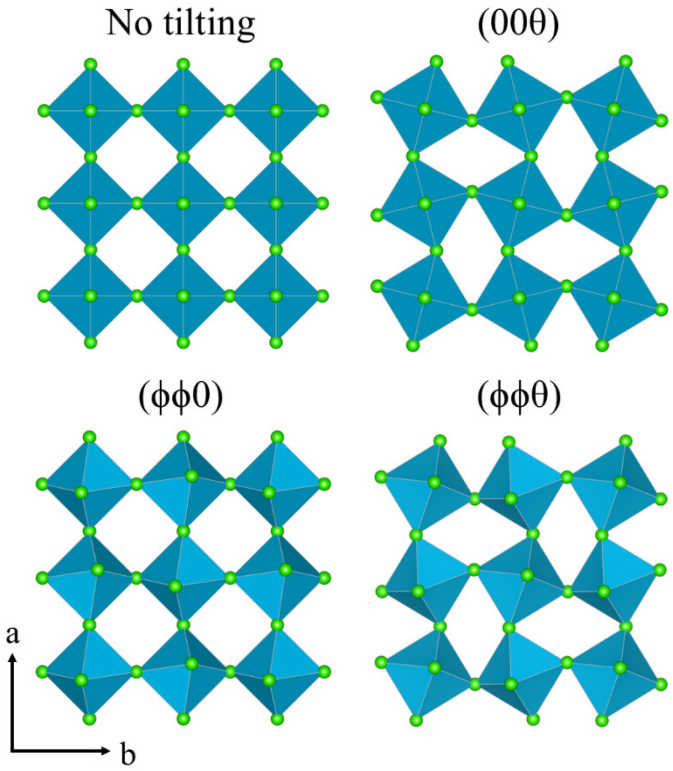

Figure 1: Common types of octahedral tilting seen in Ruddlesden-Popper phases.

The presence of cation order also has symmetry consequences, hence the space groups and unit cells associated with various types of octahedral tilting are different for cation ordered $A'_4MM'X_8$ $n = 1$ RP phases than they are for A'_2MX_4 phases. To determine the space group symmetries associated with the most common types of octahedral tilting in ordered $n = 1$ RP phases, ISODISTORT[32,33] was used to analyze combinations of rotational and occupational distortions to the Ni-centered octahedra of the K_2NiF_4 parent structure. First, various octahedral tilting patterns were applied to the K_2NiF_4 structure, following the procedure outlined by Liu at al.[1] Those subgroups were then selected as the parent structure and occupational distortions corresponding to chessboard ordering were applied. In this manner the symmetry consequences of octahedral tilting and cation ordering in $n = 1$ RP phases were mapped out and are summarized in Table 1. Although not comprehensive, the space groups for the most pertinent tilts (θ-tilts, ϕ-tilts, and the most prevalent combinations of the two) are included. It should be noted that McClure et al. previously discussed the symmetry consequences of cation ordering in $n = 1$ RP phases with various tilts.[27] In the current analysis we have standardized tilt assignments and expanded the number of tilt systems included.

Table 1: The symmetries of A'_2BX_4 RP phases and $A'_4BB'X_8$ cation ordered RP phases with common patterns of octahedral tilting. Basis vectors of each subgroup are given in terms of the parent lattice vectors of the *I*4/*mmm* parent structure.

Tilt system		**A'_2BX_4 (no cation ordering)**		**$A'_4BB'X_8$ (with cation ordering)**	
1st layer	**2nd layer**	**Space group**	**Basis vectors**	**Space group**	**Basis vectors**
000	000	*I*4/*mmm*	(1,0,0), (0,1,0), (0,0,1)	*Cmmm*	(0,0,1), (1,$\bar{1}$,0), (1,1,0)
00θ	00$\bar{\theta}$	*Cmce*	(0,0,1), (1,$\bar{1}$,0), (1,1,0)	*C*2/*m*	(1,$\bar{1}$,0), (0,0,1), ($\bar{1}$,$\bar{1}$,0)
ϕϕ0	ϕϕ0	*Cmce*	(1,$\bar{1}$,0), (0,0,$\bar{1}$), (1,1,0)	*C*2/*m*	(0,0,$\bar{1}$), (1,$\bar{1}$,0), ($\bar{1}$,$\bar{1}$,0)
ϕ00	0ϕ0	*P*4$_2$/*ncm*	(1,$\bar{1}$,0), (1,1,0), (0,0,1)	*P*2$_1$/*c*	(1,1,0), (1,$\bar{1}$,0), (0,0,$\bar{1}$)
ϕϕθ	ϕϕθ	*Pbca*	(0,0,1), (1,1,0), ($\bar{1}$,1,0)	*P*2$_1$/*c*	($\bar{1}$,1,0), (0,0,1), (1,1,0)
ϕϕθ	ϕϕ$\bar{\theta}$	*P*2$_1$/*c*	(½,–½,–½), ($\bar{1}$,$\bar{1}$,0), ($\bar{1}$,1,0)	*P*$\bar{1}$	($\bar{1}$,$\bar{1}$,0), ($\bar{1}$,1,0), (½,–½,–½)

Experimental

The following reagents were purchased and used as received: HCl (Fisher Scientific, 37%, *aq*), In_2O_3 (Alfa Aesar, 99.994%), AgBr (Alfa Aesar, 99.5+%), Bi_2O_3 (Acros Organics, 99+%), benzylamine (Acros, 99%), HBr (Acros, 48%, *aq*), H_3PO_2 (Sigma-Aldrich, 50 wt%, *aq*), $BiBr_3$ (Alfa Aesar, 99%), and phenethylamine (Acros, 99%). AgCl was precipitated from aqueous solutions of $AgNO_3$ (99.9+%, Alfa Aesar) and KCl (Certified ACS, Fisher). Benzylammonium halide and phenethylammonium halide salts were prepared by the neutralization of either benzylamine (99%, Acros Organics) or phenethylamine (99%, Acros Organics) in neat ethanol with either HCl (37%, Sigma-Aldrich) or HBr (Acros, 48%, aq).

Single crystals of $(BzA)_4AgBiBr_8$ and $(PEA)_4AgBiBr_8$ were grown hydrothermally in HBr in the presence of a small amount of H_3PO_2 to prevent the oxidation of Br^- to Br_3^-. As an example, consider the synthesis of $(BzA)_4AgBiBr_8$. First, Bi_2O_3 (0.2343 mmol, 109.2 mg) and AgBr (0.469 mmol, 88.0 mg) were weighed and added to a 23 mL Teflon liner. Next, 3.2 mL of concentrated HBr (aq, 8.65 M) and 0.4 mL H_3PO_2 (aq, 50 wt%) were added to the Teflon liner. Finally, benzylamine (2.35 mmol, 0.257 mL) was slowly added to the above solution, generating

white smoke in this neutralization process. The Teflon liner was sealed in an acid-digestion metal jacket which was then placed in an oven and set to ramp at 25 °C/h from room temperature to 100 °C, dwell at that temperature for 1 h, and then cool at 1 °C/h back to 25 °C. The synthesis of $(PEA)_4AgBiBr_8$ was performed in a similar manner. Hydrothermal syntheses of both bromides yielded single crystals but failed to produce phase pure products; common impurities included RNH_3Br and RNH_3^+–Bi^{3+}–Br^- compounds, such as $(BzA)_3BiBr_6$. The acid-assisted grinding synthesis outlined in the Supporting Information (Experimental Procedures) for $(BzA)_4AgBiBr_8$ produced a powder with small AgBr and BzABr impurities, while for $(PEA)_4AgBiBr_8$ it yielded a phase pure powder (Figure S1).

Single crystals of $(BzA)_4AgInCl_8$ and $(PEA)_4AgInCl_8$ were grown with the hydrothermal method.[29] As an example consider the synthesis of $(BzA)_4AgInCl_8$. In_2O_3 (0.5325 mmol, 147.8 mg), AgCl (1.065 mmol, 152.6 mg), BzACl (4.26 mmol, 611.8 mg), and 7.10 mL of 12 M HCl (*aq*) were added to a 23 mL Teflon cup and the solution was stirred. The Teflon cup was then loaded into an acid-digestion metal jacket, sealed, placed in a box furnace, and heated to 125 °C for 3 h before cooling down to room temperature at a rate of 5 °C/h. A mixture of the desired colorless, clear plates and a white powder were isolated from the reaction mixture, washed with diethyl ether, and dried on a vacuum filter. The synthesis of $(PEA)_4AgInCl_8$ was performed in a similar manner. Hydrothermal syntheses of both chlorides failed to produce phase pure products; common impurities included AgCl, RNH_3Cl, and RNH_3^+–In^{3+}–Cl^- compounds, such as $(BzA)_3InCl_6$. The acid-assisted grinding syntheses of $(BzA)_4AgInCl_8$ and $(PEA)_4AgInCl_8$ outlined in the Supporting Information (Experimental Procedures) produced powders with only minor AgCl impurities (Figure S1). Additional synthetic details for all four double perovskites can be found in the Supporting Information (Experimental Procedures).

Single crystals of $(BzA)_2PbBr_4$, $(PEA)_2PbBr_4$, $(BzA)_2CdCl_4$, and $(PEA)_2CdCl_4$ used for UV-visible diffuse reflectance spectroscopy (DRS) studies were grown using layered solution crystal growths as demonstrated by Mitzi for growing crystals of $(PEA)_2PbCl_4$.[34] Full synthetic details are outlined in the Supporting Information (Experimental Procedures).

Single-crystal XRD (SCXRD) studies were conducted on either a Nonius Kappa diffractometer equipped with a Bruker APEX–II CCD and Mo Kα radiation (λ = 0.71073 Å) or a Bruker D8 Venture diffractometer equipped with a Bruker PHOTON II detector and Mo Kα radiation (λ = 0.71073 Å). Crystal temperatures during data collection were controlled using an Oxford Cryosystems Cryostream. For all crystals, the data were integrated using the Bruker SAINT software program.[35] Data for $(BzA)_4AgBiBr_8$, $(BzA)_4AgInCl_8$, and $(PEA)_4AgInCl_8$ were scaled using the SADABS[36] software program, while data for $(PEA)_4AgBiBr_8$ were scaled using the TWINABS[37] software program. The crystal structures of $(BzA)_4AgBiBr_8$ and $(BzA)_4AgInCl_8$ at 295 K were solved by charge flipping using Olex2.[38] The crystal structures of $(PEA)_4AgBiBr_8$ and $(PEA)_4AgInCl_8$ were solved by intrinsic phasing using SHELXT.[39] The crystal structure of $(BzA)_4AgInCl_8$ at 100 K was solved by direct methods using ShelXS.[40] For all crystals, non-hydrogen atoms were first refined isotropically followed by anisotropic refinement by full matrix least-squares calculations based on R^2 using ShelXL.[41] Hydrogen atoms were first located in the difference map then positioned geometrically and allowed to ride on their respective parent atoms.

Powder X-ray diffraction (PXRD) data were collected using a Bruker D8 Advance diffractometer (40 kV, 40 mA; sealed Cu X-ray tube) equipped with a Johansson-type graphite monochromator and a Lynx Eye XE-T position-sensitive detector. PXRD refinements were performed using the Topas-Academic (ver. 6) software package.[42] Crystal structures were visualized with the VESTA (ver. 3) software program.[43]

Differential scanning calorimetry (DSC) was performed on a TA Instruments DSC 250 in Tzero aluminum pans. Samples were cycled between 200 K and various maximum temperatures under a nitrogen stream of 25 mL/min with heating and cooling rates of 10 K/min. Thermal gravimetric analysis (TGA) measurements were performed on a TA Instruments TGA 550 in platinum pans. Samples were heated from ambient temperature to 600 K at a rate of 10 K/min under a nitrogen stream of 25 mL/min. UV-visible DRS data were collected from 250–800 nm with a PerkinElmer Lambda 950 spectrometer equipped with a 60 mm InGaAs integration sphere. The spectrometer was calibrated by using a Labsphere Certified Reflectance Standard.

Results

Single crystal X-ray diffraction was used to determine the crystal structure of $(BzA)_4AgBiBr_8$ at 200 K and $(PEA)_4AgBiBr_8$ at 298 K. The space group symmetry, unit cell dimensions, select bond distances, bond angles, and details of the octahedral tilting are summarized in Table 2. Full details of the crystal structure determinations can be found in the Supporting Information (Table S1). Depictions of the crystal structure of each compound are shown in Figure 2.

$(BzA)_4AgBiBr_8$ exhibits $(\phi\phi\theta)/(\phi\phi\theta)$ octahedral tilting with complete ordering of Ag^+ and Bi^{3+} ions leading to $P2_1/c$ space group symmetry, consistent with the symmetry predictions given in Table 1. Our structure agrees with a previous structure determination at 300 K by Xu et al.[44] The Ag-centered octahedron exhibits a significant axial compression, with much shorter bonds between silver and the terminal (axial) bromide ions, 2×2.705(1) Å, than between silver and the bridging (equatorial) bromide ions, 2×2.960(1) Å and 2×2.963(1) Å. This type of distortion, tending toward a linear coordination environment if carried to the extreme, is known to occur for d^{10} cations like Ag^+, Au^+ and Hg^{2+}.[45] It is driven by mixing of the empty 5s and filled $4dz^2$ orbitals of the Ag^+ cation. In contrast, the Bi-centered octahedra are much less distorted with a Bi–Br distance of 2×2.874(1) Å to the terminal bromides, and 4×2.839(1) Å to the bridging bromides. Like other halide perovskites containing Bi^{3+} the doubly occupied 6s orbital on bismuth is not stereochemically active.

Xu et al. reported a reversible phase transition in $(BzA)_4AgBiBr_8$ at 387 K (upon heating) and determined the structure of $(BzA)_4AgBiBr_8$ at 393 K.[44] The high temperature structure exhibits $(00\theta)/(00\bar{\theta})$ tilting and disorder of Ag^+ and Bi^{3+} ions leading to *Cmce* space group symmetry (see Table 1). This phase transition from $P2_1/c$ to *Cmce* can be thought of as an order-disorder transition in which the ϕ-tilts and position of the BzA^+ cation become dynamic and there is loss of cation ordering between Ag^+ and Bi^{3+}. However, our DSC scans did not reveal a phase transition between 200 K and 450 K. Therefore, no high temperature diffraction data of this compound was collected in our study (Figure S2). The reason for this discrepancy is not clear.

Table 2: A summary of pertinent details regarding the crystal structures of $(BzA)_4AgBiBr_8$ and $(PEA)_4AgBiBr_8$.

Compound	**$(BzA)_4AgBiBr_8$**	**$(PEA)_4AgBiBr_8$**
Temperature (K)	200	298
Space group	$P2_1/c$	$P\bar{1}$
a (Å)	8.030(2)	11.559(1)
b (Å)	32.466(9)	11.670(1)
c (Å)	8.061(2)	17.538(1)
α (°)	90	106.113(4)
β (°)	90.023(3)	100.401(4)
γ (°)	90	90.215(3)
Volume (Å^3)	2101.5(9)	2231.9(4)
Octahedral tilt system	(ϕϕθ)/(ϕϕθ)	(ϕϕθ)/(ϕϕ$\bar{\theta}$)
Ag–Br distances (Å)*	2 × 2.705(1) (*t*) 2 × 2.960(1) (*b*) 2 × 2.963(1) (*b*)	2.654(4), 2.668(4) (*t*) 3.023(3), 3.042(3) (*b*) 3.064(4), 3.077(4) (*b*)
Bi–Br distances (Å)*	2 × 2.874(1) (*t*) 2 × 2.839(1) (*b*) 2 × 2.839(1) (*b*)	2.856(3), 2.890(3) (*t*) 2.838(3), 2.842(3) (*b*) 2.851(3), 2.858(3) (*b*)
Ag–Br–Bi bond angle (°)	157.38(4)	159.1(1), 159.3(1), 159.9(1), 161.2(1)
ϕ-tilt (°)	4.01(3), 4.35(3)	3.78(9), 3.92(9), 6.24(9), 6.63(9)
θ-tilt (°)	22.40(3), 22.51(3)	18.89(7), 19.66(7), 19.68(7), 21.04(7)

*Distances to the terminal (axial) bromides are denoted with (*t*) and those to the bridging (equatorial) bromides with (*b*).

$(PEA)_4AgBiBr_8$ adopts a $P\bar{1}$ structure with (ϕϕθ)/(ϕϕ$\bar{\theta}$) octahedral tilting and ordered PEA^+ cations at room temperature. The room temperature structure is consistent with previous structure determinations at 100 K by Schmitz et al. and 250 K by Pantaler et al.[46,47] While the other double perovskite compositions discussed in this paper have a ½ *a* + ½ *b* offset of adjacent perovskite layers, as expected for an RP phase, the structure of $(PEA)_4AgBiBr_8$ has a layer offset closer to ½ *a* + 0 *b* (Figure 2d). This type of layer shift is intermediate between the layer shift factor expected for RP (½ *a* + ½ *b*) and DJ (0 *a* + 0 *b*) phases. It is sometimes referred to as near-DJ2.[2,48] The deviation of the layer shift from the normal RP stacking does not impact the symmetry associated with (ϕϕθ)/(ϕϕ$\bar{\theta}$) octahedral tilting, as this pattern of tilting results in the same space group for either RP or DJ phases, as discussed by McNulty et al.[2] Despite $(PEA)_4AgBiBr_8$ adopting a $P\bar{1}$ structure and possessing (ϕϕθ)/(ϕϕ$\bar{\theta}$) octahedral tilting, its structure is not consistent with the symmetry predictions given in Table 1. Conformational ordering of PEA cations changes the translational symmetry of the unit cell, resulting in a doubling of the number of formula units per unit cell and an expansion of the in-plane unit cell metrics to be twice that of the *I*4/*mmm* parent cell (basis vectors of (2,0,0), (0,$\bar{2}$,0), (½,–½,–½)). Like $(BzA)_4AgBiBr_8$, the silver-centered octahedra are axially compressed and the bismuth-centered are relatively symmetric (Table 2). If anything the compression of the silver-centered octahedra is more pronounced in $(PEA)_4AgBiBr_8$. Unlike $(BzA)_4AgBiBr_8$, the Ag^+ and Bi^{3+} cations

are no longer positioned on inversion centers but on the general Wyckoff site. This allows for small distortions of the [$AgBr_6$] and [$BiBr_6$] octahedra where the intraoctahedral bond angles that would ideally be 180° and 90° range from 175.8(1)° to 179.5(1)° and from 86.5(9)° to 93.8(1)°, respectively.

Given the fact that both $A_4AgBiBr_8$ compounds display a combination of ϕ- and θ-tilts, as well as full ordering of organic cations, we do not anticipate structural phase transitions on cooling. Prior studies of $(PEA)_4AgBiBr_8$ down to 100 K support this assumption.[46,47] To look for phase transitions on heating in $(PEA)_4AgBiBr_8$, DSC data was collected from 200 K to 475 K and three reversable features are seen over this temperature range (Figure S2). In the heating curve there are two large overlapping peaks with onsets at 402 K and 408 K as well as a smaller peak with an onset at 461 K (Figure S2, Table S3). Single-crystal x-ray diffraction studies at 423 K give a primitive monoclinic unit cell with a = 8.30(1) Å, b = 8.15(1) Å, c = 18.09(3) Å, α = γ = 90°, and β = 94.35(4)° which was indexed to the $P2/m$ space group (Table S4). At 423 K the crystal diffracted poorly, especially beyond a d-spacing of 1.2 Å, likely caused by a high degree of dyanamic disorder above the phase transition. The crystal also degraded over the span of the data collection. As a result only the position of the inorganic ions and nitrogen atoms of the PEA^+ cations can be located. At 423 K this $P2/m$ structure has (ϕϕ0)/(ϕϕ0) octahedral tilting and chessboard ordering of silver and bismuth atoms (Figure S3) which does not match the $C2/m$ space group predicted from applying (ϕϕ0)/(ϕϕ0) octahedral tilting and cation ordering to the RP parent structure (Table 1). However, the $P2/m$ structure contains one ocathedral layer per unit cell and a layer shift close to 0 a + 0 b (near-DJ), therefore, this subgroup would be better related to the DJ parent structure ($TlAlF_4$) with $P4/mmm$ symmetry rather than the RP parent structure.[2] Application of (ϕϕ0)/(ϕϕ0) octahedral tilting and chessboard cation ordering to the $TlAlF_4$ DJ parent structure using ISODISTORT does result in a $P2/m$ unit cell with the basis vectors of $(1,\bar{1},0)$, (1,1,0), (0,0,1) in terms of the $P4/mmm$ parent structure, which is in agreement with our diffraction studies. Like the 298 K structure, the silver-centered octahedra are axially compressed and the bismuth-centered octahedra are relatively symmetric (Table S4). The transition of $(PEA)_4AgBiBr_8$ from $P\bar{1}$ to $P2/m$ upon heating above 408 K, corresponds to a loss of θ-tilts ((ϕϕθ)/(ϕϕ$\bar{\theta}$) to (ϕϕ0)/(ϕϕ0)) and a change in its layer shift to 0 a + 0 b (near-DJ2 → near-DJ). Due to the crystal degredation and poor data quality when collecting data at 423 K, SCXRD data were not collected above the third peak in the DSC data at 461 K. A summary of the 423 K structure can be found in the Supplemental Information (Table S4 and Figure S3).

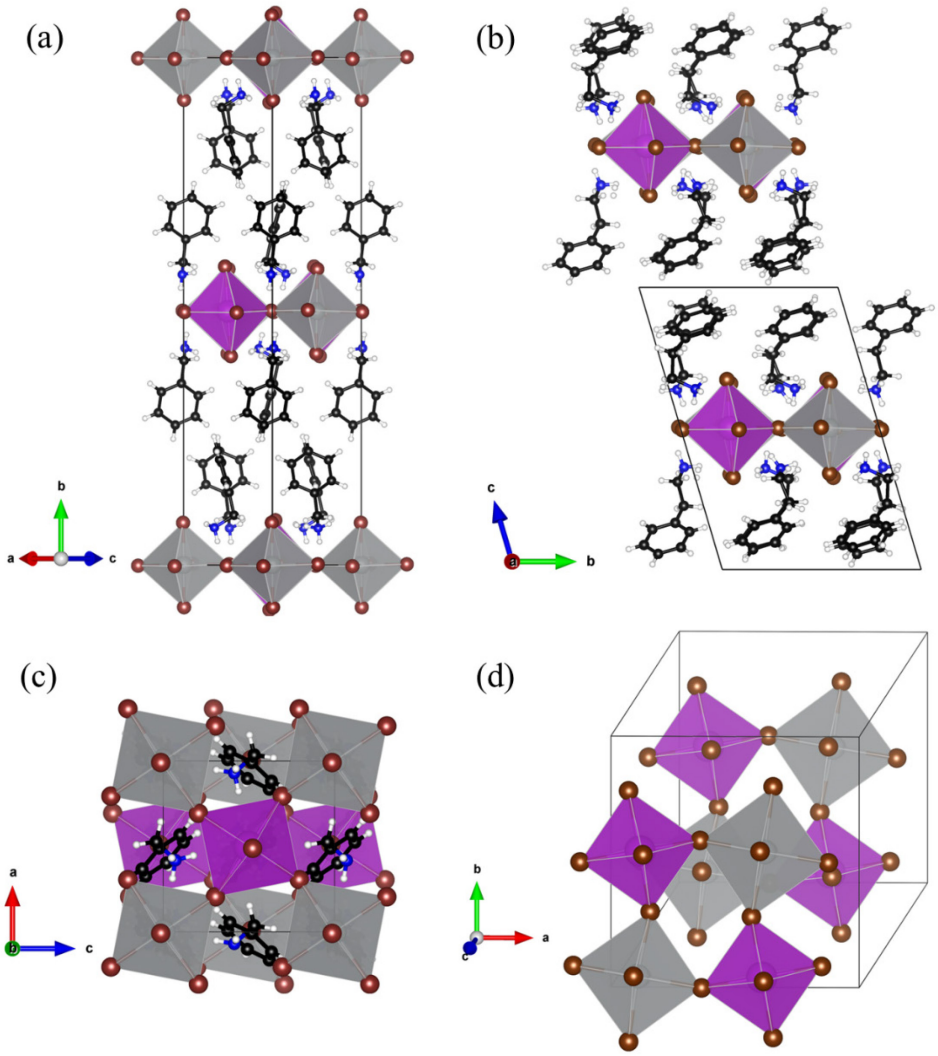

Figure 2: In-plane view of the structure of (a) $(BzA)_4AgBiBr_8$ at 200 K, (b) $(PEA)_4AgBiBr_8$ at 298 K. Top-down view of (c) $(BzA)_4AgBiBr_8$ and (d) $(PEA)_4AgBiBr_8$ (PEA cations are omitted for clarity) at the same temperatures. Bismuth-centered octahedra are shown in purple and silver-centered octahedra in silver. Maroon, blue, black and white spheres represent bromine, nitrogen, carbon, and hydrogen, respectively. Black lines denote the unit cell.

The crystal structure of $(BzA)_4AgInCl_8$ at 295 K and 100 K as well as that of $(PEA)_4AgInCl_8$ at 200 K were determined. The results are summarized in Table 3 and illustrated in Figure 3. Further details can be found in the Supporting Information (Table S2). At room temperature $(BzA)_4AgInCl_8$ adopts an n = 1 RP double perovskite structure with the space group $C2/m$. From our symmetry analysis, we can assign the structure as having $(\phi\phi0)/(\phi\phi0)$ octahedral tilting (Figure 3a and 3d). In this compound the inorganic layers consist of corner-connected octahedra, with a chessboard like ordering of silver- and indium-centered octahedra. As seen for the $A_4AgBiBr_8$ compositions already discussed, the silver-centered octahedra are axially compressed, with two short Ag−Cl bonds to the terminal chlorides of 2.520(4) Å, and four longer Ag−Cl bonds to the bridging chlorides of 2.925(2) Å, while the indium-centered octahedra are far less distorted (Table 3). In this structure, the positions of the organic cations are disordered across mirror planes, presumably due to dynamic motion of these molecular cations. DSC data reveals no observable phase transitions in $(BzA)_4AgInCl_8$ between 200 K and 400 K (Figure S2), however, single crystal

XRD data of $(BzA)_4AgInCl_8$ collected at 100 K reveals a $P\bar{1}$ structure with (ϕϕθ)/(ϕϕθ̄) octahedral tilting (Figure 3b and 3e). Thus, $(BzA)_4AgInCl_8$ must undergo a phase transition from $C2/m$ to $P\bar{1}$ somewhere between 100 K and 200 K. The transition is driven by the onset of θ-tilting and orientational ordering of BzA^+ cations. The Ag–Cl and In–Cl bond lengths in the low temperature triclinic structure are similar to those of the room temperature monoclinic structure (see Table 3).

Table 3: A summary of pertinent details regarding the crystal structures of $(BzA)_4AgInCl_8$ and $(PEA)_4AgInCl_8$.

Compound	**$(BzA)_4AgInCl_8$**	**$(BzA)_4AgInCl_8$**	**$(PEA)_4AgInCl_8$**
Temperature (K)	295	100	200
Space group	$C2/m$	$P\bar{1}$	$P2_1/c$
Octahedral tilt system	(ϕϕ0)/(ϕϕ0)	(ϕϕθ)/(ϕϕθ̄)	(ϕϕθ)/(ϕϕθ)
a (Å)	32.606(2)	7.4501(6)	7.4157(3)
b (Å)	7.5426(4)	7.5656(6)	7.4469(2)
c (Å)	7.6894(5)	16.666(1)	38.371(1)
α (°)	90	90.077(3)	90
β (°)	90.054(3)	102.884(2)	90.046(2)
γ (°)	90	90.086(2)	90
Volume (Å^3)	1891.1(2)	915.7(1)	2119.0(1)
Ag–Cl distances (Å)	2 × 2.520(4) (*t*) 4 × 2.925(1) (*b*)	2 × 2.538(3) (*t*) 2 × 2.808(5) (*b*) 2 × 2.846(5) (*b*)	2 × 2.570(5) (*t*) 2 × 2.816(3) (*b*) 2 × 2.864(3) (*b*)
In–Cl distances (Å)	2 × 2.540(4) (*t*) 4 × 2.492(1) (*b*)	2 × 2.542(4) (*t*) 2 × 2.553(5) (*b*) 2 × 2.556(5) (*b*)	2 × 2.530(5) (*t*) 2 × 2.473(4) (*b*) 2 × 2.502(3) (*b*)
Ag–Cl–In bond angle (°)	167.41(7)	159.4(1), 162.9(1)	159.7(1), 162.3(1)
ϕ-tilt (°)	11.42(7)	10.7(1), 12.2(1)	11.8(1), 11.9(1)
θ-tilt (°)	0	11.3(1), 11.6(1)	12.1(1), 12.2(1)

*Distances to the terminal (axial) chlorides are denoted with (*t*) and those to the bridging (equatorial) chlorides with (*b*).

$(PEA)_4AgInCl_8$ adopts an n = 1 RP double perovskite structure with the space group $P2_1/c$ and (ϕϕθ)/(ϕϕθ) octahedral tilting at 200 K (Figure 3c and 3f).[49] The coordination environments of Ag^+ and In^{3+} in this structure are similar to those seen in $(BzA)_4AgInCl_8$, however, the axial compression of the silver-centered octahedron isn't as pronounced in this compound (Table 3). DSC data of $(PEA)_4AgInCl_8$ from 200 K to 400 K reveals a phase transition at 343 K upon heating (Figure S2). SCXRD data of $(PEA)_4AgInCl_8$ collected above the phase transition at 375 K gives a body centered tetragonal unit cell with $a = b = 5.35(1)$ Å, $c = 38.7(1)$ Å, and $\alpha = \beta = \gamma = 90°$. The only body centered tetragonal unit cell with the n = 1 RP structure is the parent (aristotype) structure with $I4/mmm$ space group symmetry, in which there is neither In/Ag cation ordering nor octahedral tilting (Table 1). At 375 K the crystal diffracted poorly, especially beyond a d-spacing of 1.15 A, which is likely due to the high degree of dynamic disorder in the structure. Consequently, only the nitrogen and first carbon atom of the highly disordered PEA^+ cation could be located. The transition of $(PEA)_4AgInCl_8$ to the $I4/mmm$ structure above 343 K, corresponds to a

loss of ϕ- and θ-tilts, dynamical disorder in the PEA^+ cations, and possibly incoherent stacking of inorganic layers which manifests as a mixed occupancy metal site. However, the similar scattering factors of the isoelectronic Ag^+ and In^{3+} make the diffraction peaks associated solely with cation ordering very weak. It is concievable that the cation ordering is retained at high temperature, but the low quality of the diffraction data make it difficult to observe such weak peaks. A summary of the 375 K structure can be found in the Supplemental Information (Table S4 and Figure S3).

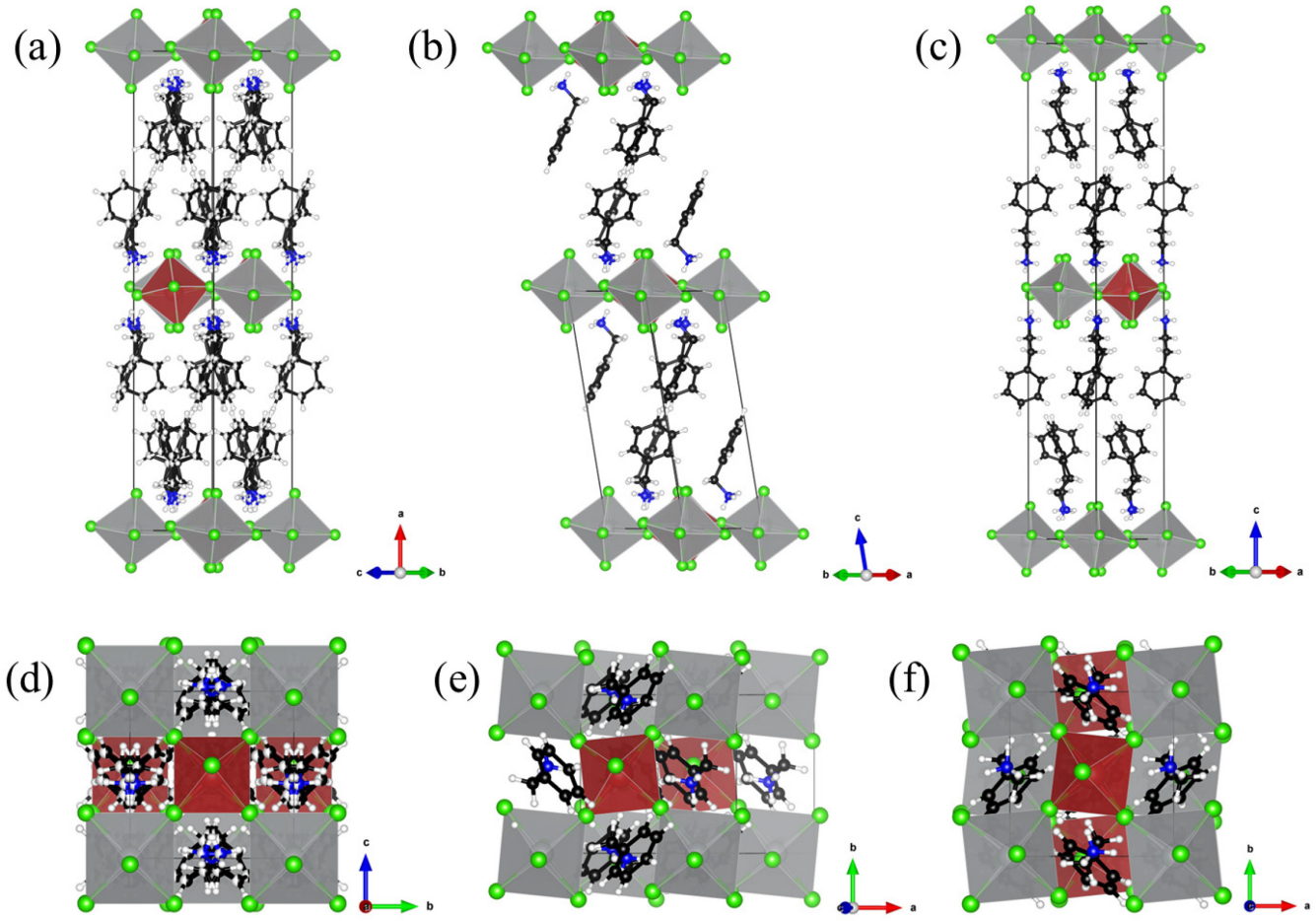

Figure 3: In-plane view of (a) $(BzA)_4AgInCl_8$ at 295 K, (b) $(BzA)_4AgInCl_8$ at 100 K, (c) $(PEA)_4AgInCl_8$ at 200 K. Top-down view of (d) $(BzA)_4AgInCl_8$, (e) $(BzA)_4AgInCl_8$, and (f) $(PEA)_4AgInCl_8$ at the same temperatures. Indium-centered octahedra are shown in red and silver-centered octahedra in silver. Green, blue, black and white spheres represent chlorine, nitrogen, carbon and hydrogen, respectively. In all parts, black lines denote the unit cell.

TGA data shows that each of the four hybrid double perovskites is stable up to approximately 450–500 K, before mass is lost via decomposition (Figure S4). For a given set of cations the bromide composition is stable up to somewhat higher temperatures than the chloride. Comparing compounds containing the same inorganic fragments, those compounds containing PEA^+ are stable to higher temperatures than those containing BzA^+.

Diffuse reflectance data were collected on powders of the four double perovskites and transformed to absorbance using the Kubelka-Munk equation (Figure 4). Although we cannot definitely assign the nature of their band gaps, based on previous band structure studies of similar compounds, we assume direct band gaps for $(BzA)_4AgBiBr_8$ and $(PEA)_4AgBiBr_8$, and indirect band gaps for $(BzA)_4AgInCl_8$ and $(PEA)_4AgInCl_8$.[28,47,50] Tauc plots estimate the

band gaps of $(BzA)_4AgBiBr_8$, $(PEA)_4AgBiBr_8$, $(BzA)_4AgInCl_8$, and $(PEA)_4AgInCl_8$ to be 2.46 eV, 2.51 eV, 3.94 eV, and 3.82 eV, repsectively (Figure S5). These band gaps are similar to those previously reported for n = 1 RP double perovskites by Mao et al. and McClure et al.; 2.41−2.65 eV for $A'_4AgBiBr_8$ compounds and 3.96−4.27 eV for $A'_4AgInCl_8$ compounds.[27,28] Although Xu et al. assigned $(BzA)_4AgBiBr_8$ an indirect band of 2.29 eV using a Tauc plot, the absorption onset in our data is consistent with their UV-visible absorption data.[44] Absorbance studies of $(PEA)_4AgBiBr_8$ thin films were conducted by Schmitz et al. and Pantaler et al. showing absorption onsets between 2.6 and 2.7 eV.[46,47] The band gaps of the four $A'_4AgBiBr_8$ and $A'_4AgInCl_8$ double perovskites are 0.5 to 0.7 eV smaller than their A'_2PbBr_4 and A'_2CdCl_4 single perovskite derivatives (Figure S5). While the band gaps seen for $A'_4AgInCl_8$ compounds are too large for photovoltaic applications, the $A'_4AgBiBr_8$ compounds do absorb an appreciable amount of visible light.

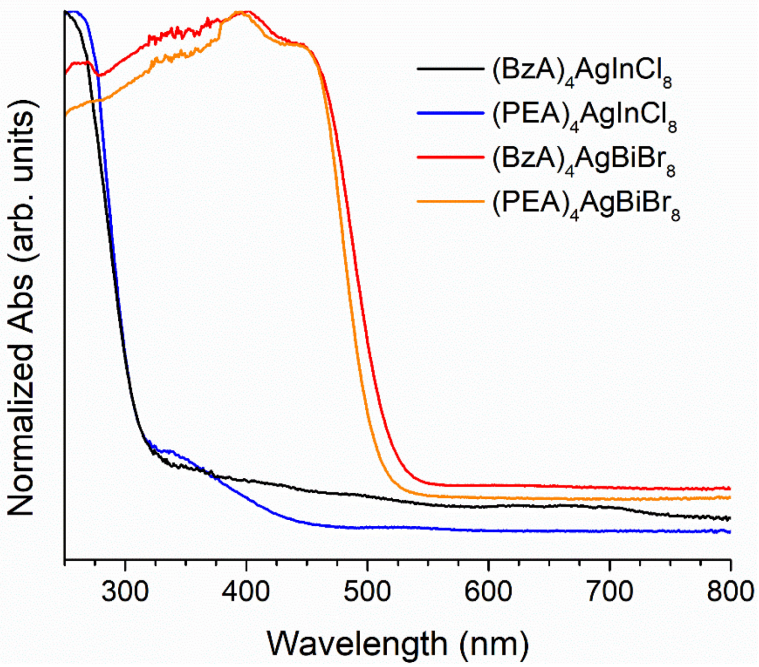

Figure 4: Absorbance data of $(BzA)_4AgBiBr_8$, $(PEA)_4AgBiBr_8$, $(BzA)_4AgInCl_8$, and $(PEA)_4AgInCl_8$ at room temperature.

Discussion

We begin our discussion with a closer look at the bonding within the inorganic layers. The first thing to note is the chessboard ordering of Ag^+ and Bi^{3+}/In^{3+} ions. The ordering is maintained not only within the layers, but there is also a coherent stacking of ordered layers. While cation ordering is uncommon in all-inorganic RP phases, it seems to be normal for hybrid halide RP phases, such as $(propylammonium)_4AgInCl_8$,[28] $(butylammonium)_4AgBiBr_8$,[29] $(phenethylammonium)_4NaFeCl_8$,[7] and $(phenethylammonium)_4CuInCl_8$[51]. Detecting cation ordering in n = 1 RP double perovskites from PXRD data has proven challenging.[27] For instance, laboratory PXRD collected on a powder sample of $(PEA)_4AgBiBr_8$ made by acid-assisted grinding shows negligible intensity in the (111) cation ordering peak, whereas this peak is clearly present in SCXRD data. Resolving cation ordering from PXRD data becomes even more difficult with cations with similar scattering powers, like isoelectronic Ag^+ and In^{3+} ([Kr] $4d^{10}$

$5s^0$), occupying the octahedral sites. This emphasizes the importance of SCXRD data in detecting cation ordering in hybrid $n = 1$ RP phases.

One factor that helps stabilize cation ordering is the pronounced difference in the coordination environments of Ag^+ and Bi^{3+}/In^{3+} cations. The Ag–X bonds to the terminal halide ions are compressed while those to the bridging halide ions are elongated, making for a coordination environment that might be described as intermediate between octahedral and linear. This distortion makes the terminal halide ions chemically inequivalent and may have consequences for hydrogen bonding interactions with the organic cations. This type of distortion is not seen for Ag^+ in three-dimensional halide double perovskites like $Cs_2AgBiBr_6$ and $Cs_2AgInCl_6$, but has been observed in other layered hybrid perovskites like (propylammonium)$_4AgInCl_8$ and (butylammonium)$_4AgBiBr_8$.[29] Bond valence calculations given in the Supporting Information (Table S5) produce bond valence sums for the inorganic cations that are generally within 10% of their expected values of 1.00 (Ag^+) and 3.00 (Bi^{3+}/In^{3+}), indicative of stable coordination environments.

Next, we consider the packing of the organic cations. In both (BzA)$_4AgBiBr_8$ and (BzA)$_4AgInCl_8$, the benzylammonium cations are aligned nearly perpendicular to the inorganic layers and pack in an edge-to-face manner producing a herringbone pattern commonly seen in the crystal structures of acenes (Figure 5).[52,53] This arrangement is thought to be stabilized by dispersion interactions between the electron-poor hydrogen atoms of the phenyl ring with the electron-rich π clouds of the neighboring BzA^+ cations. The limited number of conformational degrees of freedom of the BzA^+ cation makes it unable to form other types of phenyl–phenyl interactions, such as π–π stacking, while maintaining favorable hydrogen bonding interactions with the inorganic layers. The intra-layer edge-to-face packing seen in both double perovskites is also found in (BzA)$_2PbX_4$ (X = Cl, Br, I)[10,54,55] and (BzA)$_2CdCl_4$[56]. Much like a traditional hydrogen bond, the strength of the CH–π edge-to-face interaction is dictated by 1) the distance between the hydrogen atom on one phenyl ring and the plane of an adjacent phenyl ring, and 2) the angle between the carbon and hydrogen on one phenyl ring and the centroid of an adjacent phenyl ring. Shorter distances and angles closer to 180° are indicative of stronger interactions. In (BzA)$_4AgBiBr_8$ at 200 K , the distances and angles range from 3.617 Å to 3.694 Å and from 139.28° to 142.98°, respectively. In (BzA)$_4AgInCl_8$ at 100 K, the distances and angles range from 3.252 Å to 3.306 Å and from 143.44° to 145.66°, respectively.

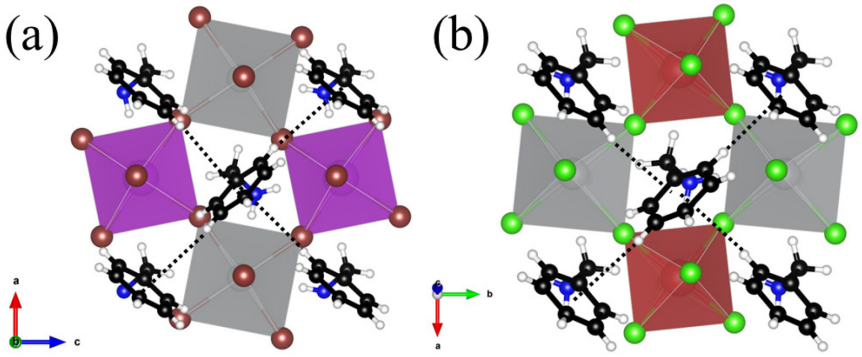

Figure 5: CH–π interactions between (a) (BzA)$_4AgBiBr_8$ at 200 K, (b) (BzA)$_4AgInCl_8$ at 100 K. Silver-centered octahedra are shown in silver, bismuth-centered octahedra in purple, and indium-centered octahedra in red. Maroon, green, blue, black, and white spheres represent bromine, chlorine, nitrogen, carbon, and hydrogen, respectively. Dotted lines represent CH–π interactions between phenyl rings of adjacent BzA^+ cations.

The presence of an extra $–CH_2–$ group gives the phenethylammonium cation more conformational flexibility than benzylammonium, as illustrated in Figure 6. In the anti (extended) conformation, the ethylammonium tail extends away from the phenyl ring and the N–C1–C2–C3 dihedral angle is close to 180°. This configuration minimizes intramolecular steric interactions and is the conformation taken by neutral PEA molecules in the solid state, as well as PEA^+ cations in phenethylammonium bromide.[57,58] In the gauche (folded) conformation, the ammonium head group of ethylammonium tail folds towards the phenyl ring and the N–C1–C2–C3 dihedral angle is close to 60°. The gauche conformation can be classified as "left-handed" or "right-handed" in a Newman projection, depending upon whether the ethylammonium fragment points to the left or right, respectively.[34]

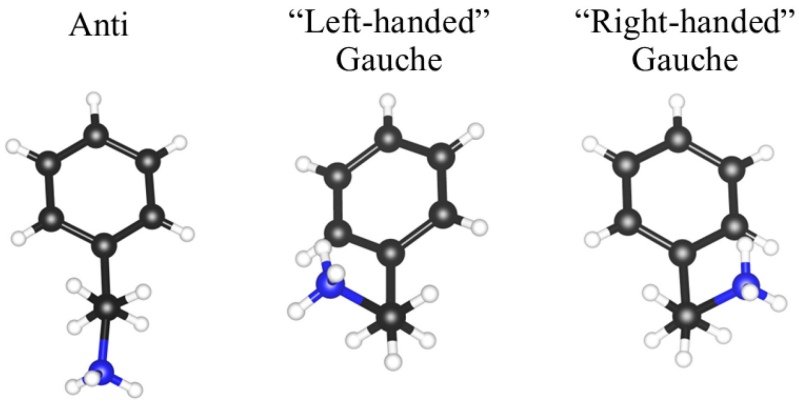

Figure 6: Newman projections down the C1–C2 bond axis of the phenethylammonium cation showing the different possible conformations.

In the hybrid RP compounds studied, the conformations of the PEA^+ cations vary with the size of the inorganic layer. To a first approximation, the organic cations can be thought to occupy a cuboid in which the base is a parallelogram defined by four neighboring inorganic cations ($a \times b$ for the parent *I*4/*mmm* structure) and the height is half the distance from one layer to the next (c/4 for the parent *I*4/*mmm* structure). In $(PEA)_4AgInCl_8$ which has more compact inorganic layers (cuboid basal area = 27.61 $Å^2$), the PEA^+ cations adopt the anti conformation (dihedral angles 168(1)° and 173(1)°) and form intra-layer edge-to-face interactions similar to what is seen for the benzylammonium cations discussed above (Figure 7a and 7c). However, in $(PEA)_4AgBiBr_8$ which has a larger inorganic layer (cuboid basal area = 33.80 $Å^2$), three of the four PEA^+ cations in the unit cell adopt a gauche conformation (dihedral angles 62(3)°, 62(4)° and 67(3)°), while the fourth PEA^+ cation takes an anti conformation (dihedral angle 172(3)°). Instead of the intra-layer edge-to-face interactions seen in the three other compounds studied here, the phenyl rings adopt a slip-stacked packing arrangement (Figure 7b and 7d) within each organic layer, and weak edge-to-face interactions between layers. In $(PEA)_4AgBiBr_8$ at 298 K, the inter-layer H–phenyl ring distances and C–H–phenyl ring angles range from 3.189 Å to 3.694 Å and from 119.69° to 126.61°, respectively. Interestingly in the $(PEA)_2PbX_4$ (X = Cl, Br, I) single perovskites with larger inorganic layers (cuboid basal areas ranging from 31.07 $Å^2$ to 37.70 $Å^2$), PEA^+ molecules exclusively adopt gauche conformations, and form similar weak inter-layer edge-to-face interactions with a slip stacking pattern within each layer.[59–61] As the basal dimensions of the inorganic layer increase, the distances between PEA^+ cations must also increase if the intra-layer

edge-to-face packing of the aromatic phenyl rings is maintained. When this distance becomes too long it apparently becomes more favorable for the PEA^+ cations to take a gauche conformation and pack differently. Presumably this packing also disrupts the ½ *a* + ½ *b* layer stacking of archetypal RP phase in favor of the ½ *a* + 0 *b* stacking seen for $(PEA)_4AgBiBr_8$ at 298 K.

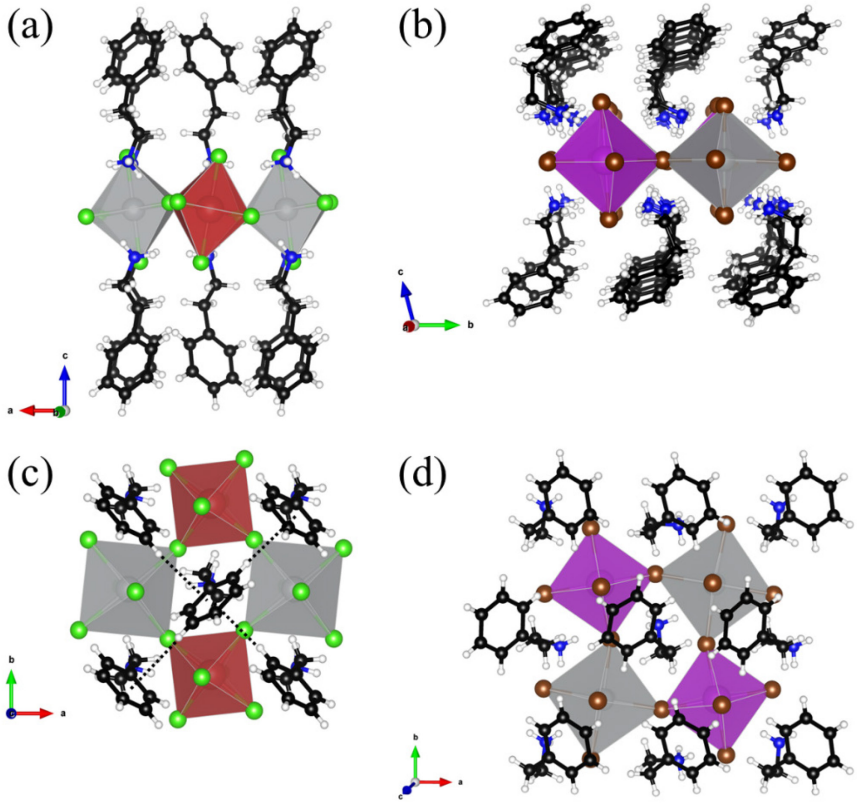

Figure 7: Edge-to-face packing of PEA^+ cations in $(PEA)_4AgInCl_8$ at 200 K as shown by (a) an in-plane view and (c) a top-down view showing CH–π interactions (dotted lines) between phenyl rings of adjacent PEA^+ cations. Slip-stack packing of PEA^+ cations in $(PEA)_4AgBiBr_8$ at 298 K as shown by an (b) in-plane view and (d) top-down view. Silver-centered octahedra are shown in silver, bismuth-centered octahedra in purple, and indium-centered octahedra in red. Maroon, green, blue, black, and white spheres represent bromine, chlorine, nitrogen, carbon, and hydrogen, respectively.

Finally, we come to the hydrogen bonding interactions that drive octahedral tilting and play a critical role in the competition between polar and non-polar structures. The θ-tilts can be estimated by subtracting 90° from the largest interior angle of the parallelogram defined by neighboring cations in the inorganic layer (see Figure S6). They are large in both $(BzA)_4AgBiBr_8$ at 200 K and $(PEA)_4AgBiBr_8$ at 298 K (Table 2). The presence of θ-tilts reduces the lateral dimensions of the inorganic layers and alters the distances between halide ions and the ammonium head group of the neighboring organic cations. Even larger θ-tilts, ranging from 28° to 36°, are seen at room temperature for $(BzA)_2PbCl_4$ and $(BzA)_2PbBr_4$ (Table S6). At the same time the ϕ-tilts, which can be estimated from the Br–Ag–Bi–Br dihedral angles (see Figure S6), are rather small in both $A'_4AgBiBr_8$ compositions. This is visually apparent in Figure 2 by noting that the Ag^+ and Bi^{3+} ions are nearly co-planar with the bridging Br^- ions.

The situation changes significantly in $(BzA)_4AgInCl_8$ and $(PEA)_4AgInCl_8$, where the ϕ- and θ-tilts are of comparable magnitude in the low temperature structure (see Table 3). The ϕ-tilts push the bridging halides out of the plane containing the inorganic cations and simultaneously move the terminal halides closer to one of the four

neighboring $–NH_3^+$ groups. This distortion facilitates the formation of shorter, stronger hydrogen bonds to the terminal halide ions, as discussed in reference 1. Hydrogen bond lengths and angles for the four cation-ordered RP phases reported here can be found in the Supporting Information (Table S7). Visual depictions of hydrogen bonding in BzA- and PEA-containing RP phases discussed in this paper can also be found in the Supporting Information (Figure S7 and Figure S8).

One of the goals of the current study was to prepare new hybrid layered halide ferroelectrics that do not contain toxic elements like lead and cadmium. Unfortunately, all the crystal structures discussed thus far are centrosymmetric, ruling out the possibility of ferroelectricity. This begs the question, why don't the double perovskites studied here adopt polar crystal structures like their pseudo-ternary A_2PbBr_4 and A_2CdCl_4 analogs? The answer to this question largely comes down to differences in the orientations of the polar $–NH_3^+$ ends of the organic cations, and to understand these differences we must examine the hydrogen bonding interactions between the organic cations and the inorganic layers more closely.

Given its superior ferroelectric properties, a comparison with $(BzA)_2PbCl_4$ (T_C = 438 K, P_s = 13 μC·cm^{-2}) is particularly apt. The structure of $(BzA)_4AgBiBr_8$ is the most similar to that of $(BzA)_2PbCl_4$. Both feature large θ-tilts, edge-to-face packing of the aromatic phenyl rings, and similar lateral dimensions of the inorganic layers—the cuboid basal area is 30.24 Å^2 for $(BzA)_2PbCl_4$ and 32.4 Å^2 for $(BzA)_4AgBiBr_8$. Above its Curie temperature, $(BzA)_2PbCl_4$ exhibits (00θ)/(00$\bar{\theta}$) tilting and the positions of the BzA^+ cations are disordered, leading to *Cmce* space group symmetry. On cooling below T_C, it undergoes a transition to the polar $Cmc2_1$ space group which is driven by orientational ordering of the BzA^+ cations. The best way to visualize the dipole moments created by orientational ordering of the BzA^+ cations is to view the interactions of the $–CH_2NH_3^+$ head groups with a single inorganic layer, as shown in Figure 8. The strongest hydrogen bonds are formed with the terminal chloride ions, and each BzA^+ cation forms hydrogen bonds with two such ions. The large θ-tilts act to contract the lateral dimensions of the inorganic layer and pull the chlorides closer to the $–CH_2NH_3^+$ head groups, the hydrogen bonding distances are further optimized by displacements of the chloride ions toward two BzA^+ cations. The $–CH_2NH_3^+$ groups align with exactly the same pattern of hydrogen bonding above and below the inorganic layer, retaining the mirror plane that bisects the layer. In the image shown in Figure 8a one-half of the $–CH_2NH_3^+$ groups point to the right, the [011] direction, and the other half point upward, the [0$\bar{1}$1] direction. This destroys the inversion center present on the inorganic cations in the high temperature structure and leads to the creation of a polar axis along the [001] direction. The displacements of the terminal chloride ions distort the octahedra, leading to a Cl–Pb–Cl bond angle of 167.9(1)°.[10]

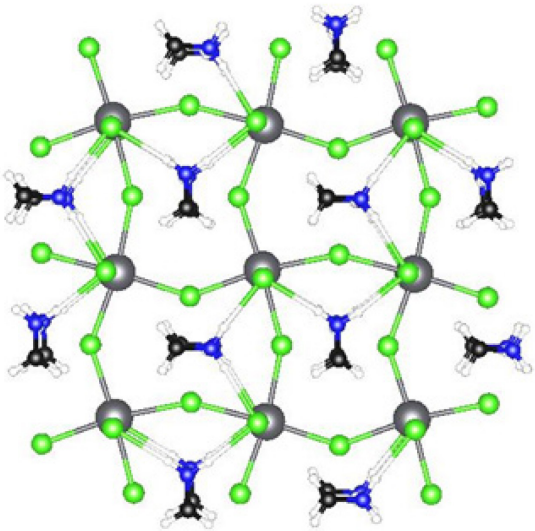

(a) $(BzA)_2PbCl_4$

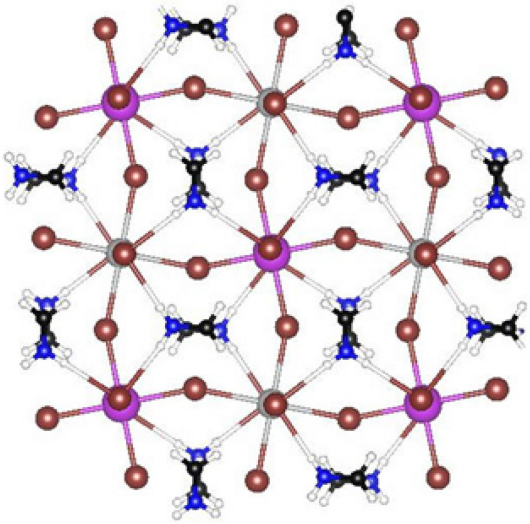

(b) $(BzA)_4AgBiBr_8$

Figure 8: A top-down view showing the hydrogen bonding interactions between BzA^+ cations above and below a single inorganic layer in (a) $(BzA)_2PbCl_4$ at 293 K[10] and (b) $(BzA)_4AgBiBr_8$ at 200 K. For clarity only the $CH_2NH_3^+$ head of the organic cation and hydrogen bonds made with terminal halides are shown. Dark grey, silver, purple, green, maroon, blue, black, and white spheres represent lead, silver, bismuth, chlorine, bromine, nitrogen, carbon, and hydrogen, respectively.

A similar view of $(BzA)_4AgBiBr_8$ reveals a critical difference (Figure 8b). Each BzA^+ cation still forms two hydrogen bonds to terminal bromide ions, but for a given octahedron those hydrogen bonds pull the bromide ions on the upper and lower sides of the inorganic layer in opposite directions. This distortion creates the small ϕ-tilts of 4.01(3)° and 4.35(3)° that are present in $(BzA)_4AgBiBr_8$, but absent in $(BzA)_2PbCl_4$. This pattern of hydrogen bonding retains the inversion centers at the Ag^+ and Bi^{3+} centers and leads to an antiparallel alignment in the orientation of the $–CH_2NH_3^+$ groups above and below the plane. Hence, the local dipole moments cancel and there is no possibility of ferroelectricity. Like $(BzA)_2PbCl_4$, $(BzA)_4AgBiBr_8$ has been reported to undergo a phase transition at high temperature to a structure with $(00\theta)/(00\bar{\theta})$ tilting and positionally disordered BzA^+ cations.[44]

Given the otherwise similar crystal structures, what is responsible for the different patterns of hydrogen bonding seen in $(BzA)_4AgBiBr_8$ and $(BzA)_2PbCl_4$? While it is difficult to answer this question definitively, a possible answer lies in the fact that the low temperature centrosymmetric structure of $(BzA)_4AgBiBr_8$ does not require a distortion of the metal-centered octahedra. The Br–Ag–Br and Br–Bi–Bi bond angles involving the terminal bromides are strictly linear by symmetry. The axial compression of the Ag-centered octahedra, driven by $5s - 4dz^2$ mixing, favors a linear Br–Ag–Br bond, while the presence of a filled 6s orbital on Pb^{2+} could help facilitate the out-of-center distortion seen the lead octahedron in $(BzA)_2PbCl_4$.[62]

How does the situation change when ϕ-tilts become more dominant as is the case for $(BzA)_4AgInCl_8$? To answer this question, it is instructive to compare the structures of $(BzA)_2CdCl_4$ and $(BzA)_4AgInCl_8$. The former adopts a (ϕϕ0)/(ϕϕ0) pattern of octahedral tilting. Symmetry analysis predicts that this pattern of octahedral tilting in an n = 1 RP phase should result in a *Cmce* structure (Table 1), but at room temperature the space group symmetry is *C*2*ce*.[56] Much like $(BzA)_2PbCl_4$ the symmetry is lowered by orientational ordering of the BzA^+ cations and polar distortions of the Cd-centered octahedra. Although there is no mirror plane bisecting the inorganic layer, the $–CH_2NH_3^+$ groups are all pointed either down or to the left, both above and below the inorganic layer (Figure 9a) and therefore do not cancel out. Hydrogen bonds pull the terminal chlorides either upward or to the right leading to a distortion of the octahedron. The distortion is comparable to the distortion seen in $(BzA)_2PbCl_4$, with a Cl–Cd–Cl bond angle of 169.63(3)°.

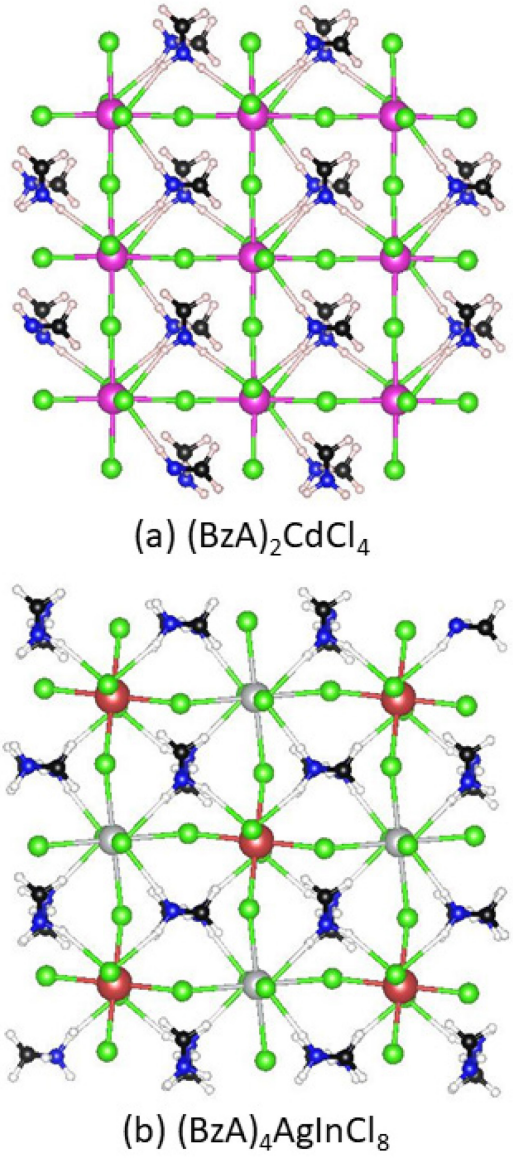

Figure 9: A top-down view showing the hydrogen bonding interactions between BzA^+ cations above and below a single inorganic layer in (a) $(BzA)_2CdCl_4$ at 298 K[56] and (b) $(BzA)_4AgInCl_8$ at 100 K. For clarity only the $–CH_2NH_3^+$ head of the organic cation and hydrogen bonds made with terminal halides are shown. Pink, silver, red, green, blue, black, and white spheres represent cadmium, silver, indium, chlorine, nitrogen, carbon, and hydrogen, respectively.

In $(BzA)_4AgInCl_8$ the hydrogen bonds above and below the inorganic layer pull the terminal chloride ions in opposite directions, much like they do in $(BzA)_4AgBiBr_8$ (Figure 9b). This retains the inversion centers that lie on the Ag^+ and In^{3+} positions and the net movement of the terminal chloride ions is consistent with the positions expected from the interplay of ϕ- and θ-tilts. One can speculate that here also the unfavorability of distorting the Cl–Ag–Cl away from linear may be responsible for tipping the delicate balance of structure directing forces in favor of the nonpolar structure with (ϕϕθ)/(ϕϕ$\bar{\theta}$) tilting.

Conclusions

The hybrid layered perovskites $(BzA)_4AgBiBr_8$, $(PEA)_4AgBiBr_8$, $(BzA)_4AgInCl_8$, $(PEA)_4AgInCl_8$ have been successfully synthesized from hydrothermal methods and structurally characterized using single crystal XRD methods. In all four compounds the inorganic layers exhibit a chessboard ordering of Ag^+ and Bi^{3+}/In^{3+} and the layers stack in a coherent pattern that maintains the ordering over three-dimensional space. The octahedra surrounding Ag^+ show a large axial compression, which results in much shorter bonds to the terminal halide ions than to the bridging halide ions, whereas the bismuth- and indium-centered octahedra show only small distortions.

$(BzA)_4AgBiBr_8$ and $(BzA)_4AgInCl_8$ feature similar conformations and packing of BzA^+ cations. In each structure the phenyl rings are oriented nearly perpendicular to the inorganic layers and they interact through intra-layer edge-to-face contacts, producing a herringbone-like packing of these nearly planar molecular cations. A similar pattern is seen in $(PEA)_4AgInCl_8$, where the more flexible PEA^+ cation adopts an anti conformation. However, in $(PEA)_4AgBiBr_8$ the expanded lateral dimensions of the inorganic layer destabilize this mode of packing. In this composition, three-fourths of the PEA^+ adopt a gauche (folded) conformation and the organic cations adopt a slip-stacked packing that gives rise to parallel phenyl rings. The change in packing of the organic layers seen in $(PEA)_4AgBiBr_8$ at 298 K alters the offset or shift of the inorganic layers from the ½ *a* + ½ *b* characteristic of the Ruddlesden-Popper structure to approximately ½ *a* + 0 *b*.

Hydrogen bonding interactions between the organic and inorganic layers lead to pronounced octahedral tilting in these compounds. All four compositions show either $(\phi\phi\theta)/(\phi\phi\theta)$ or $(\phi\phi\theta)/(\phi\phi\bar{\theta})$ octahedral tilting at low temperature and adopt non-polar space groups. This differs from the analogous pseudo-ternary compounds like $(BzA)_2PbCl_4$ and $(BzA)_2CdCl_4$, where distortions of the metal-centered octahedra stabilize hydrogen bonding patterns that lead to polar structures. For hybrid *n* = 1 RP phases, the combination of ϕ- and θ-tilts stabilizes hydrogen bonding interactions that produce an antipolar alignment of the dipole moments of the organic cations. We hypothesize that the pseudo-linear environment of the Ag^+ cations may inhibit octahedral distortions and favor the combination of ϕ- and θ-tilting. At higher temperatures ϕ-tilts have been reported to become dynamic in $(BzA)_4AgBiBr_8$[44], though for reasons that are not clear that phase transition is not seen in our experiments. In both $(PEA)_4AgBiBr_8$ and $(BzA)_4AgInCl_8$, the θ-tilts become dynamic at high temperature, while both ϕ- and θ-tilts become dynamic in $(PEA)_4AgInCl_8$.

A symmetry analysis shows that octahedral tilting alone cannot lead to a polar structure in *n* = 1 cation ordered RP phases. The additional distortions that produce a polar structure in some A'_2MX_4 phases, like $(BzA)_2PbCl_4$, appear to be unfavorable in the hybrid *n* = 1 RP double perovskites. Therefore, the design of polar hybrid layered double perovskites for ferroelectricity requires alternate strategies. Possibilities include adding substituents to the organic molecules to enhance dipole–dipole interactions and thereby promote polar organic packing or moving to *n* = 2 RP phases where it is known that octahedral tilting alone can produce a polar structure.[63,64]

ASSOCIATED CONTENT

Supporting Information: Additional synthetic details; Pawley fits of powder X-ray diffraction data; summaries of single crystal X-ray diffraction data; differential scanning calorimetry data; thermal gravimetric analysis data; absorbance data and Tauc plots; bond valence sum calculations; definition of octahedral tilting magnitude; hydrogen bond distances and angles; depictions of hydrogen bonding (DOC)

INFORMATION

Corresponding Author

*E-mail: woodward.55@osu.edu

ORCID

Joseph T. Race: 0000-0002-8551-3627
Tianyu Liu: 0000-0002-2537-4231
Patrick M. Woodward: 0000-0002-3441-2148

Author Contributions

ε These authors contributed equally. The manuscript was written through the contributions of all authors. All authors have given approval to the final version of the manuscript.

Notes

The authors declare no competing financial interest.

ACKNOWLEDGMENT

Funding for J.T.R., T.L., and P.M.W. was provided by the National Science Foundation under Award DMR-2003793. We thank Dr. Curtis Moore for his help mounting crystals for high-temperature single crystal x-ray diffraction studies as well as his discussions and guidance on single crystal x-ray diffraction, and Dr. Branton Campbell for useful discussions on the symmetry analysis and use of ISODISTORT.

REFERENCES

(1) Liu, T.; Holzapfel, N. P.; Woodward, P. M. Understanding structural distortions in hybrid layered perovskites with the n = 1 Ruddlesden–Popper structure. *IUCrJ* **2023**, *10* (4), 385–396.

(2) McNulty, J. A.; Lightfoot, P. Structural chemistry of layered lead halide perovskites containing single octahedral layers. *IUCrJ* **2021**, *8* (4), 485–513.

(3) Era, M.; Morimoto, S.; Tsutsui, T.; Saito, S. Organic-inorganic heterostructure electroluminescent device using a layered perovskite semiconductor $(C_6H_5C_2H_4NH_3)_2PbI_4$. *Appl. Phys. Lett.* **1994**, *65* (6), 676–678.

(4) Li, R.; Yi, C.; Ge, R.; Zou, W.; Cheng, L.; Wang, N.; Wang, J.; Huang, W. Room-temperature electroluminescence from two-dimensional lead halide perovskites. *Appl. Phys. Lett.* **2016**, *109* (15), 151101.

(5) Park, S.-H.; Oh, I.-H.; Park, S.; Park, Y.; Kim, J. H.; Huh, Y.-D. Canted antiferromagnetism and spin reorientation transition in layered inorganic–organic perovskite $(C_6H_5CH_2CH_2NH_3)_2MnCl_4$. *Dalton Trans.* **2012**, *41*, 1237-1242.

(6) Vishnoi, P.; Zuo, J. L.; Li, X.; Binwal, D. C.; Wyckoff, K. E.; Mao, L.; Kautzsch, L.; Wu, G.; Wilson, S. D.; Kanatzidis, M. G.; Seshadri, R.; Cheetham, A. K. Hybrid Layered Double Perovskite Halides of Transition Metals. *J. Am. Chem. Soc.* **2022**, *144* (15), 6661–6666.

(7) Xue, J.; Wang, Z.; Comstock, A.; Wang, Z.; Sung, H. H. Y.; Williams, I. D.; Sun, D.; Liu, J.; Lu, H. Chemical Control of Magnetic Ordering in Hybrid Fe−Cl Layered Double Perovskites. *Chem. Mater.* **2022**, *34* (6), 2813–2823.

(8) Seo, J.; McGillicuddy, R. D.; Slavney, A. H.; Zhang, S.; Ukani, R.; Yakovenko, A. A.; Zheng, S. L.; Mason, J. A. Colossal barocaloric effects with ultralow hysteresis in two-dimensional metal–halide perovskites. *Nat. Commun.* **2022**, *13* (1), 2536.

(9) Li, J.; Barrio, M.; Dunstan, D. J.; Dixey, R.; Lou, X.; Tamarit, J.-L.; Phillips, A. E.; Lloveras, P.; Li, J.; Dunstan, D. J.; Dixey, R.; Phillips, A. E.; Lou, X.; Barrio, M.; Tamarit, J.-L.; Lloveras, P. Colossal Reversible Barocaloric Effects in Layered Hybrid Perovskite $(C_{10}H_{21}NH_3)_2MnCl_4$ under Low Pressure Near Room Temperature. *Adv. Funct. Mater.* **2021**, *31* (46), 2105154.

(10) Liao, W. Q.; Zhang, Y.; Hu, C. L.; Mao, J. G.; Ye, H. Y.; Li, P. F.; Huang, S. D.; Xiong, R. G. A lead-halide perovskite molecular ferroelectric semiconductor. *Nat. Commun.* **2015**, *6*, 7338.

(11) Rao, W.; Li, M.; You, X.; Wei, Z.; Zhang, M.; Wang, L.; Cai, H. The Role of Fluorine-Substituted Positions on the Phase Transition in Organic–Inorganic Hybrid Perovskite Compounds. *Inorg. Chem.* **2021**, *60* (19), 14706–14712.

(12) Lee, J. K.; Hong, K. S.; Jang, J. W. Roles of Ba/Ti Ratios in the Dielectric Properties of $BaTiO_3$ Ceramics. *J. Am. Ceram. Soc.* **2001**, *84* (9), 2001–2006.

(13) Soares, M. R.; Senos, A. M. R.; Mantas, P. Q. Phase coexistence region and dielectric properties of PZT ceramics. *J. Eur. Ceram. Soc.* **2000**, *20* (3), 321–334.

(14) Masuda, Y.; Masumoto, H.; Baba, A.; Goto, T.; Hirai, T. Crystal growth, dielectric and polarization reversal properties of $Bi_4Ti_3O_{12}$ single crystal. *Jpn. J. Appl. Phys.* **1992**, *31* (9S), 3108–3112.

(15) Subbarao, E. C. A family of ferroelectric bismuth compounds. *J. Phys. Chem. Solids* **1962**, *23* (6), 665–676.

(16) Sun, Z.; Liu, X.; Khan, T.; Ji, C.; Asghar, M. A.; Zhao, S.; Li, L.; Hong, M.; Luo, J. A Photoferroelectric Perovskite-Type Organometallic Halide with Exceptional Anisotropy of Bulk Photovoltaic Effects. *Angew. Chem. Int. Ed.* **2016**, *55* (22), 6545–6550.

(17) Ji, C.; Dey, D.; Peng, Y.; Liu, X.; Li, L.; Luo, J. Ferroelectricity-Driven Self-Powered Ultraviolet Photodetection with Strong Polarization Sensitivity in a Two-Dimensional Halide Hybrid Perovskite. *Angew. Chem. Int. Ed.* **2020**, *59* (43), 18933–18937.

(18) Wang, C. F.; Li, H.; Li, M. G.; Cui, Y.; Son, X.; Wang, Q. W.; Jiang, J. Y.; Hua, M. M.; Xu, Q.; Zhao, K.; Ye, H. Y.; Zhang, Y. Centimeter-Sized Single Crystals of Two-Dimensional Hybrid Iodide Double Perovskite $(4,4\text{-Difluoropiperidinium})_4AgBiI_8$ for High-Temperature Ferroelectricity and Efficient X-Ray Detection. *Adv. Funct. Mater.* **2021**, *31* (13), 2009457.

(19) Zheng, W.; Wang, X.; Zhang, X.; Chen, B.; Suo, H.; Xing, Z.; Wang, Y.; Wei, H.; Chen, J.; Guo, Y.; Wang, F. Emerging Halide Perovskite Ferroelectrics. *Adv. Mater.* **2023**, *35* (21), 2205410.

(20) Li, S.; Birol, T. Suppressing the ferroelectric switching barrier in hybrid improper ferroelectrics. *npj Comput. Mater.* **2020**, *6* (1), 168.

(21) Liu, M.; Zhang, Y.; Lin, L. F.; Lin, L.; Yang, S.; Li, X.; Wang, Y.; Li, S.; Yan, Z.; Wang, X.; Li, X. G.; Dong, S.; Liu, J. M. Direct observation of ferroelectricity in $Ca_3Mn_2O_7$ and its prominent light absorption. *Appl. Phys. Lett.* **2018**, *113* (2), 022902.

(22) Oh, Y. S.; Luo, X.; Huang, F. T.; Wang, Y.; Cheong, S. W. Experimental demonstration of hybrid improper ferroelectricity and the presence of abundant charged walls in $(Ca,Sr)_3Ti_2O_7$ crystals. *Nat. Mater.* **2015**, *14* (4), 407–413.

(23) Mcclure, E. T.; Ball, M. R.; Windl, W.; Woodward, P. M. Cs_2AgBiX_6 (X = Br, Cl): New Visible Light Absorbing, Lead-Free Halide Perovskite Semiconductors. *Chem. Mater.* **2016**, *28* (5), 1348–1354.

(24) Volonakis, G.; Amir, †; Haghighirad, A.; Milot, R. L.; Sio, W. H.; Filip, M. R.; Wenger, B.; Johnston, M. B.; Herz, L. M.; Snaith, H. J.; Giustino, F. $Cs_2InAgCl_6$: A New Lead-Free Halide Double Perovskite with Direct Band Gap. *J. Phys. Chem. Lett.* **2017**, *8* (4), 772–778.

(25) Sun, Y.; José Fernández-Carrión, A.; Liu, Y.; Yin, C.; Ming, X.; Liu, B.-M.; Wang, J.; Fu, H.; Kuang, X.; Xing, X. Bismuth-Based Halide Double Perovskite $Cs_2LiBiCl_6$: Crystal Structure, Luminescence, and Stability. *Chem. Mater.* **2021**, *33* (15), 5905–5916.

(26) Vargas, B.; Rodriguez-Lopez, G.; Solis-Ibarra, D. The Emergence of Halide Layered Double. *ACS Energy Lett.* **2020**, *5* (11), 3591–3608.

(27) Mcclure, E. T.; Mccormick, A. P.; Woodward, P. M. Four Lead-Free Layered Double Perovskites with the n = 1 Ruddlesden − Popper Structure. *Inorg. Chem.* **2020**, *59* (9), 6010-6017.

(28) Mao, L.; Teicher, S. M. L.; Stoumpos, C. C.; Kennard, R. M.; Decrescent, R. A.; Wu, G.; Schuller, J. A.; Chabinyc, M. L.; Cheetham, A. K.; Seshadri, R. Chemical and Structural Diversity of Hybrid Layered Double Perovskite Halides. *J. Am. Chem. Soc.* **2019**, *141* (48), 19099–19109.

(29) Connor, B. A.; Leppert, L.; Smith, M. D.; Neaton, J. B.; Karunadasa, H. I. Layered Halide Double Perovskites: Dimensional Reduction of $Cs_2AgBiBr_6$. *J. Am. Chem. Soc.* **2018**, *140* (15), 5235–5240.

(30) Hatch, D. M.; Stokes, H. T.; Aleksandrov, K. S.; Misyul, S. V; Kirenskii, L. V. Phase transitions in the perovskitelike A_2BX_4 structure. *Phys. Rev. B* **1989**, *39* (13), 9282–9288.

(31) Aleksandrov, K. S.; Beznosikov, B. V.; Misyul, S. V. Successive Phase Transitions in Crystals of K_2MgF_4-Type Structure. *Phys. Status Solidi A* **1987**, *104* (2), 529–543.

(32) Stokes, H. T.; Hatch, D. M.; Campbell, B. J. *ISODISTORT*, ISOTROPY Software Suite, iso.byu.edu.

(33) Campbell, B. J.; Stokes, H. T.; Tanner, D. E.; Hatch, D. M. ISODISPLACE: An Internet Tool for Exploring Structural Distortions. *J. Appl. Cryst.* **2006**, *39* (4), 607-614.

(34) Mitzi, D. B. A Layered Solution Crystal Growth Technique the Crystal Structure of $(C_6H_5C_2H_4NH_3)_2PbCl_4$. *J. Solid State Chem.* **1999**, *145* (2), 694–704.

(35) *SAINT Version 8*; Bruker AXS Inc.: Madison, Wisconsin, USA. 2016.

(36) *SADABS Version 2016/2*; Bruker AXS Inc.: Madison, Wisconsin, USA. 2016.

(37) *TWINABS Version 2012/1*; Bruker AXS Inc.: Madison, Wisconsin, USA. 2012.

(38) Dolomanov, O. V; Bourhis, L. J.; Gildea, R. J.; Howard, J. A. K.; Puschmann, H. OLEX2: a complete structure solution, refinement and analysis program. *J. Appl. Cryst.* **2009**, *42* (2), 339–341.

(39) Sheldrick, G. M. SHELXT – Integrated space-group and crystal-structure determination. *Acta Cryst. A* **2015**, *71* (1), 3–8.

(40) Shledrick, G. SHELXS. University Of Göttingen. 2008.

(41) Sheldrick, G. M. Crystal structure refinement with SHELXL. *Acta Cryst. C* **2015**, *71* (1), 3–8.

(42) Coelho, A. A. TOPAS and TOPAS-Academic: an optimization program integrating computer algebra and crystallographic objects written in C++. *J. Appl. Cryst.* **2018**, *51* (1), 210–218.

(43) Momma, K.; Izumi, F. VESTA 3 for three-dimensional visualization of crystal, volumetric and morphology Data. *J. Appl. Cryst.* **2011**, *44* (6), 1272–1276.

(44) Xu, P.; Ye, H.; Yao, Y.; Zhu, T.; Luo, J. Lead-Free Double Perovskite Semiconductor with Rigid Spacer-Induced High-Tc Dielectric Switch Features. *Chem. Eur. J.* **2023**, *29* (40), e202300667.

(45) Burdett, J. K. *Chemical Bonding in Solids*; Oxford University Press, 1995; pp 219-269.

(46) Schmitz, F.; Horn, J.; Dengo, N.; Sedykh, A. E.; Becker, J.; Maiworm, E.; Bélteky, P.; Kukovecz, Á.; Gross, S.; Lamberti, F.; Müller-Buschbaum, K.; Schlettwein, D.; Meggiolaro, D.; Righetto, M.; Gatti, T. Large Cation Engineering in Two-Dimensional Silver−Bismuth Bromide Double Perovskites. *Chem. Mater.* **2021**, *33* (12), 4688-4700.

(47) Pantaler, M.; Diez-Cabanes, V.; Queloz, V. I. E.; Sutanto, A.; Schouwink, P. A.; Pastore, M.; García-Benito, I.; Nazeeruddin, M. K.; Beljonne, D.; Lupascu, D. C.; Quarti, C.; Grancini, G. Revealing Weak Dimensional Confinement Effects in Excitonic Silver/Bismuth Double Perovskites. *JACS Au* **2022**, *2* (1), 136–149.

(48) Tremblay, M. H.; Bacsa, J.; Zhao, B.; Pulvirenti, F.; Barlow, S.; Marder, S. R. Structures of $(4\text{-Y-}C_6H_4CH_2NH_3)_2PbI_4$ {Y = H, F, Cl, Br, I}: Tuning of Hybrid Organic Inorganic Perovskite Structures from Ruddlesden-Popper to Dion-Jacobson Limits. *Chem. Mater.* **2019**, *31* (16), 6145–6153.

(49) For the (ϕϕθ)/(ϕϕθ) octahedral tilting pattern, the order in which the irreducible representations (irrep.) responsible for ϕ- and θ-tilts are applied to the *I*4/*mmm* RP parent structure affect the basis vectors of the resulting subgroups. If the irrep responsible for (ϕϕ0)/(ϕϕ0) tilting is applied first, followed by the irreps responsible for (00θ)/(00$\bar{\theta}$) tilting and cation ordering the basis vectors of the resulting $P2_1/c$ unit cell are ($\bar{1}$,1,0), (0,0,1), (1,1,0). However, if the irrep responsible for (00θ)/(00$\bar{\theta}$) tilting is applied first, followed by the irreps responsible for (ϕϕ0)/(ϕϕ0) tilting and cation ordering the basis vectors of the resulting $P2_1/c$ unit cell are (1,$\bar{1}$,0), (1,1,0), (0,0,1). The basis vectors are unaffected by the order in which the irrep responsible for cation ordering is applied.

(50) Connor, B. A.; Su, A. C.; Slavney, A. H.; Leppert, L.; Karunadasa, H. I. Understanding the evolution of double perovskite band structure upon dimensional reduction. *Chem. Sci.* **2023**, *14* (42), 11858–11871.

(51) Aubrey, M. L.; Saldivar Valdes, A.; Filip, M. R.; Connor, B. A.; Lindquist, K. P.; Neaton, J. B.; Karunadasa, H. I. Directed assembly of layered perovskite heterostructures as single crystals. *Nature* **2021**, *597* (7876), 355–359.

(52) Anthony, J. E. Functionalized Acenes and Heteroacenes for Organic Electronics. *Chem. Rev.* **2006**, *106* (12), 5028–5048.

(53) Anthony, J. E.; Anthony, J. E. The Larger Acenes: Versatile Organic Semiconductors. *Angew. Chem. Int. Ed.* **2008**, *47* (3), 452–483.

(54) Zhang, H. Y.; Zhang, Z. X.; Song, X. J.; Chen, X. G.; Xiong, R. G. Two-Dimensional Hybrid Perovskite Ferroelectric Induced by Perfluorinated Substitution. *J. Am. Chem. Soc.* **2020**, *142* (47), 20208–20215.

(55) Mao, L.; Tsai, H.; Nie, W.; Ma, L.; Im, J.; Stoumpos, C. C.; Malliakas, C. D.; Hao, F.; Wasielewski, M. R.; Mohite, A. D.; Kanatzidis, M. G. Role of Organic Counterion in Lead- and Tin-Based Two-Dimensional Semiconducting Iodide Perovskites and Application in Planar Solar Cells. *Chem. Mater.* **2016**, *28* (21), 7781–7792.

(56) Jin, Y.; Yu, C.-H.; Zhang, W.; Jin, Y. U. Structural diversity of a series of chlorocadmate(II) and chlorocuprate(II) complexes based on benzylamine and its N-methylated derivatives. *J. Coord. Chem.* **2014**, *67* (7), 1156–1173.

(57) Weintraub, H. J. R.; Hopfinger, A. J. Conformational analysis of some phenethylamine molecules. *J. Theor. Biol.* **1973**, *41* (1), 53–75.

(58) Rademeyer, M. 2-Phenylethylammonium Bromide. *Acta Cryst. E: Struct. Rep. Online* **2007**, *63* (1), o221–o223.

(59) Di, J.; Li, H.; Chen, L.; Zhang, S.; Hu, Y.; Sun, K.; Peng, B.; Su, J.; Zhao, X.; Fan, Y.; Lin, Z.; Hao, Y.; Gao, P.; Zhao, K.; Chang, J. Low Trap Density Para-F Substituted 2D PEA_2PbX_4 (X = Cl, Br, I) Single Crystals with Tunable Optoelectrical Properties and High Sensitive X-Ray Detector Performance. *Research* **2022**, *2022*.

(60) Shibuya, K.; Koshimizu, M.; Nishikido, F.; Saito, H.; Kishimoto, S. Poly[bis(phenethylammonium) [di-bromido-Plumbate(II)]-di-μ-bromido]]. *Acta Cryst. E: Struct. Rep. Online* **2009**, *65* (11), m1323–m1324.

(61) Febriansyah, B.; Koh, T. M.; Lekina, Y.; Jamaludin, N. F.; Bruno, A.; Ganguly, R.; Shen, Z. X.; Mhaisalkar, S. G.; England, J. Improved Photovoltaic Efficiency and Amplified Photocurrent Generation in Mesoporous n = 1 Two-Dimensional Lead-Iodide Perovskite Solar Cells. *Chem. Mater.* **2019**, *31* (3), 890–898.

(62) Fu, Y.; Jin, S.; Zhu, X.-Y. Stereochemical expression of ns^2 electron pairs in metal halide perovskites. *Nat. Rev. Chem.* **2021**, *5*, 838–852.

(63) Guo, W.; Liu, X.; Han, S.; Liu, Y.; Xu, Z.; Hong, M.; Luo, J.; Sun, Z. Room-Temperature Ferroelectric Material Composed of a Two-Dimensional Metal Halide Double Perovskite for X-Ray Detection. *Angew. Chem. Int. Ed.* **2020**, *59* (33), 13879–13884.

(64) Aleksandrov, K. S.; Bartolome, J. Octahedral Tilt Phases in Perovskite-like Crystals with Slabs Containing an Even Number of Octahedral Layers. *J. Phys.: Condens. Matter* **1994**, *6*, 8219–8235.

For Table of Contents Use Only

Manuscript title: Structure directing forces in hybrid layered double perovskites containing aromatic organic cations

Authors: Joseph T. Race, Tianyu Liu, and Patrick M. Woodward

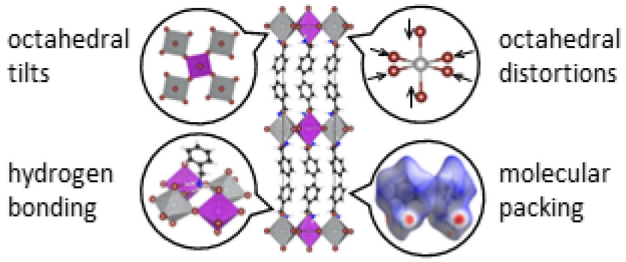

Synopsis: Synthesis, crystal structure solution, symmetry analysis, and optical characterization of four hybrid layered double perovskites containing aromatic organic cations.